Journal of Porous Materials
https://doi.org/10.1007/s10934-026-01933-y

Dual-functional $Bi_2(Se_0 0.8\ S_{0\cdot2})_3$@C composite for high-performance supercapacitors and visible-light photocatalytic MB degradation

A. Parveen[1] · N. Surumbarkuzhali[2] · D. Anitha Kumari[3] · R. Kanimozhi[4] · Arumugam Krishnan Arulmozhi[5]

Received: 12 March 2026 / Accepted: 5 June 2026
© The Author(s), under exclusive licence to Springer Science+Business Media, LLC, part of Springer Nature 2026

Abstract
The development of stable, high-density electrode materials for use in advanced electrochemical energy storage systems is of utmost importance. This study presents a simple one-step chemical precipitation approach for the fabrication of $Bi_2(Se_{0.8}S_{0.2})_3$@C, a sulfur-modified bismuth selenide solid solution coupled with amorphous carbon. The presence of crystalline bismuth selenosulfide was verified through structural investigation. Morphological analysis revealed a network of nanosheets embedded within a carbon matrix, facilitating enhanced charge transfer and providing abundant electroactive sites. Electrochemical testing in a 3 M KOH electrolyte showed that the $Bi_2(Se_{0.8}S_{0.2})_3$@C electrode achieved a specific capacitance of 950 F g^{-1} at 1 A g^{-1} and exhibited excellent cycling stability, retaining 98% of its capacitance after 5000 cycles with nearly 100% efficiency. An asymmetric supercapacitor device, using activated carbon as the negative electrode and $Bi_2(Se_{0.8}S_{0.2})_3$@C as the positive electrode, delivered a maximum energy density of 65 Wh kg^{-1} at 877 W kg^{-1} and 35 Wh kg^{-1} at 3117 W kg^{-1}. Furthermore, after just 20 s of charging, two ASC coin cells connected in series were able to power multiple LEDs for approximately 10 min, demonstrating excellent power delivery and rapid energy storage capability. These results indicate that asymmetric supercapacitors based on sulfur-modified bismuth selenide–carbon composite electrodes can be highly effective. In addition, $Bi_2(Se_0 0.8\ S_{0.2})_3$@C shows enhanced photocatalytic performance with ~92% MB degradation, higher rate constant (0.0761 min^{-1}), and excellent stability over five cycles due to improved charge separation.

Keywords Bismuth selenosulfide composite · Amorphous carbon hybrid · Asymmetric supercapacitor · Energy storage materials

1 Introduction

The increased energy demand all over the world puts requirements on energy storage systems like efficiency and environmental friendliness. There is a growing demand for storage systems that can rapidly deliver significant quantities of energy as the number of electric automobiles, portable electronics and sustainable energy sources increases. Thus, there is a need for sophisticated electrochemical energy storage systems to sustain the present technological facilities and to provide a steady supply of energy [1–3]. Electrochemical capacitors, fuel cells and batteries are the most investigated technologies nowadays. Conventional batteries may store large amounts of energy, but they often suffer from poor charging kinetics and low cycle life. Because of their rapid charge-discharge behavior, high power capability, and extended operational life, electrochemical capacitors, also

✉ A. Parveen
parveenphy26@gmail.com

1 PG & Research Department of Physics, AVS College of Arts & Science (Autonomous), Ramalingapuram, Salem, Tamilnadu 636106, India

2 PG & Research Department of Physics, Government Arts college, Salem, Tamilnadu 636007, India

3 Department of Management Studies, Vels Institute of Science, Technology and Advanced Studies (VISTAS), Chennai, Tamilnadu 600 117, India

4 Department of Chemistry, S. A Engineering College (Autonomous), Chennai, Tamilnadu 600077, India

5 Department of Mathematics, R.M.K College of Engineering and Technology, Puduvoyal, Thiruvallur, Tamilnadu 601206, India

Published online: 15 June 2026

known as supercapacitors, hold great promise for future uses for energy storage [4–6].

In fact, supercapacitors store energy by two fundamental processes of electrostatic charge buildup and programmable surface redox reactions. These mechanisms are responsible for EDLC, pseudocapacitor, and hybrid supercapacitor [7]. Graphite, activated carbon, and carbon nanotubes are instances of carbonaceous substances which are frequently present in EDLC systems. Energy storage in these systems is due to the formation of an electrical double layer at the interface between the electrodes and electrolyte. EDLCs have a low energy density, which restricts their applications in large energy storage networks, but nonetheless demonstrate exceptional cycle stability and power efficiency. Instead, pseudocapacitors are based on electrochemically active chalcogenides, hydroxide compounds, and transition metal oxides that include fast Faradaic redox reactions. These materials can provide a higher energy density and a significantly larger capacitance because of their reversible charge storage behavior [8–10].

Transition metal chalcogenides with special electrical properties, layered structures and excellent electrochemical activity are promising candidates of pseudocapacitive materials. Bismuth-based chalcogenides have been extensively studied as anode materials due to their high theoretical charge storage ability, good electrical conductivity, and chemical stability [11, 12]. The compounds have the generic formula $Bi_2\times_3$, where X=S, Se or Te. Bismuth selenide (Bi_2Se_3) is a layered semiconductor with a rhombohedral crystal form that consists of quintuple atomic layers bound by weak van der Waals contacts. Among several advantages, the design provides a larger surface area, improved accessibility of electrolyte ions and greater effectiveness of electrochemical reactions [13]. These features make Bi_2Se_3 an attractive candidate material for the electrodes of supercapacitor devices and have attracted a significant amount of research. Nanostructured Bi_2Se_3 materials have been reported to show promising capacitive performance due to the existence of electrochemically active sites and relatively high electrical conductivity [14]. Furthermore, Bi_2Se_3 has good electronic transport properties and a small band gap, indicating fast electron transportation and better electrochemical performance as revealed by theoretical studies [15].

However, the actual usage of pure Bi_2Se_3 electrodes is hindered by a variety of problems. Some of these problems are related to the limited ion mobility in bulk particles, the structural accumulation during prolonged electrochemical cycling, and the relatively low electrical conductivity compared to carbon materials. These limits may limit the total capacitance and rate capacity of the electrode material [16]. Because of its superior electrical conductivity, large specific surface area, and structural adaptability, Bi2Se3 and amorphous carbon are ideal materials for conductive purposes. This integration offers a possible solution to these issues. One method to enhance electron mobility and accelerate electrochemical reaction kinetics is to introduce amorphous carbon into the Bi_2Se_3 framework. This will generate a conductive perpetual matrix. In addition, the carbon matrix provides more active sites for charge storage, prevents the agglomeration of particles and improves the structural stability upon repeated cycling [17–20].

Bismuth-based chalcogenide ($Bi_2\times_3$) is unique because to its layered structure, high theoretical capacity, and promising electrical properties. Bi_2S_3 nanosheets have been reported to achieve a specific capacitance of 272.9 Fg^{-1} in microsupercapacitors [21] and to offer a specific capacitance of 457 Fg^{-1} by pseudocapacitive processes [22]. A well-known way to increase these properties is chalcogen alloying. It modifies the electronic band structure, introduces active sites and enhances electrical conductivity by substituting sulphur with selenium or selenium with sulphur [23].

Herein, we present a new approach to improve electrochemical characteristics of bismuth chalcogenide electrodes using a combination of structural engineering and compositional tuning. The simple one-step precipitation approach was used to successfully embed the mixed chalcogenide compound $Bi_2(Se_{0.8}S_{0.2})_3$ into an amorphous carbon matrix. The carbon skeleton has a dual function, providing a persistent conductive pathway and impeding particle aggregation across multiple cycles. This material possesses abundant accessible electroactive sites and shortens the ion transport pathways by constructing a network of interconnected nanosheets. The electrode has excellent cycling stability (~100% coulombic efficiency and 98% of the initial capacitance after 5000 cycles) and a high specific capacitance of 950 Fg^{-1} at 1 Ag^{-1}. The fabricated asymmetric supercapacitor device additionally maintains 35 Wh kg^{-1} at a higher power density of 3117 W kg^{-1} and also an energy density of 65 Wh kg^{-1} at a power density of 877 W kg^{-1}. Moreover, $Bi_2(Se_{0.8}S_{0.2})_3$@C exhibits better photocatalytic activity with ~92% MB degradation, higher rate constant (0.0761 min^{-1}) and superior stability over five cycles owing to improved charge separation.

2 Experimental details

2.1 Materials

Bismuth nitrate pentahydrate ($Bi(NO_3)_3.5H_2O$), thiourea (NH_2CSNH_2), potassium iodide (KI), potassium hydroxide (KOH), Acetic acid, selenium powder, hydrazine hydrate, ethanol, N-methyl-2-pyrrolidone (NMP), acetylene black and polyvinylidene difluoride (PVDF) were purchased from Sigma Aldrich and SD fine.

2.2 Preparation of $Bi_2(Se_{0.8}S_{0.2})_3$@C

To a transparent solution (Solution A), 0.485 g of $Bi(NO_3)_3.5H_2O$ was dissolved in 50 mL distilled water. The solution was heated to 120 °C with steady stirring to ensure thorough mixing. Solution B was prepared by dissolving the appropriate amount of thiourea with 0.34 g KI in 50 mL distilled water. Solution C was prepared by thoroughly dissolving selenium powder in hydrazine hydrate. Solution A was added dropwise to Solutions B and C with steady stirring. The method was maintained at 120 °C for 5 h following addition of acetic acid to get the pH of the mixture to about 1-1.2. Following the reaction, the product was collected by centrifugation and washed many times with distilled water and ethanol to eliminate the contaminants. Finally, the product was dried at 60 °C for 8 h to generate the $Bi_2(Se_{0.8}S_{0.2})_3$@C composite. Figure 1. Schematic of synthesis procedure. $Bi_2(Se_{0.8}S_{0.2})_3$@C is prepared via a specific process with a template. Bi^{3+} first interacts with iodide ions to create stacked BiOI nanosheets. Then, selenium and sulfur source provide Se^{2-} and S^{2-} ions. These ions eventually substitute the O_2^-/I^- ions in the structure of BiOI to create $Bi_2(Se_{0.8}S_{0.2})_3$@C while maintaining the sheet shape. Simultaneously, thiourea and hydrazine decomposition yields a thin carbon layer that uniformly coats the nanosheets. This can be summarized by the following chemical reaction.

$$Bi^{3+} + I^- \rightarrow BiOI$$
$$BiOI + Se^{2-} + S^2 \rightarrow Bi_2(Se_{0.8}S_{0.2})_3 + I^- + O^{2-}$$
$$Organic\ species \rightarrow C\ (amorphous)$$

This pathway explains the preservation of morphology along with the formation of a conductive hybrid structure.

2.3 Electrode preparation

The electrode was prepared by mixing acetylene black, $Bi_2(Se_{0.8}S_{0.2})_3$@C, and PVDF at a ratio of 80:10:10, respectively. A homogeneous paste was prepared by dispersing 8 mg of the active agent, 1 mg of carbon and 1 mg of binder in N-methyl-2-pyrrolidone (NMP). A clean stainless-steel substrate of ~1 cm^{-2} was coated. The resulting slurry was oven-dried at 60 °C for 1 h to evaporate the solvent and assure the adequate adherence. Keep the active ingredient mass loading at 2-2.5 mgcm-2. In particular, the reported capacitance values are calculated exclusively on the basis of the mass of the active material and do not take into account the impact of the binder and conductive carbon.

2.4 Electrochemical measurements

Electrochemical workstations (CHI 660E, CH Instruments, USA) examined electrode materials' electrochemical performance. All investigations used a three-electrode cell with 3 M KOH electrolyte. 2.3 Working electrode prep Sect. 2.3 covers functioning electrode preparation. The reference electrode was Ag/AgCl and the counter electrode Pt wire. Electrode material redox behavior and charge storage mechanism were studied using cyclic voltammetry (CV) at scan speeds from 10 to 100 mVs-1 within a given potential range. Galvanostatic charge-discharge (GCD) investigations examined charge-discharge behavior, rate capabilities, and specific capacitance on the same potential window at current densities from 1 to 5 A g−1. Using 5 mV amplitude electrochemical impedance spectroscopy (EIS) data from 0.01 Hz to 100 kHz.

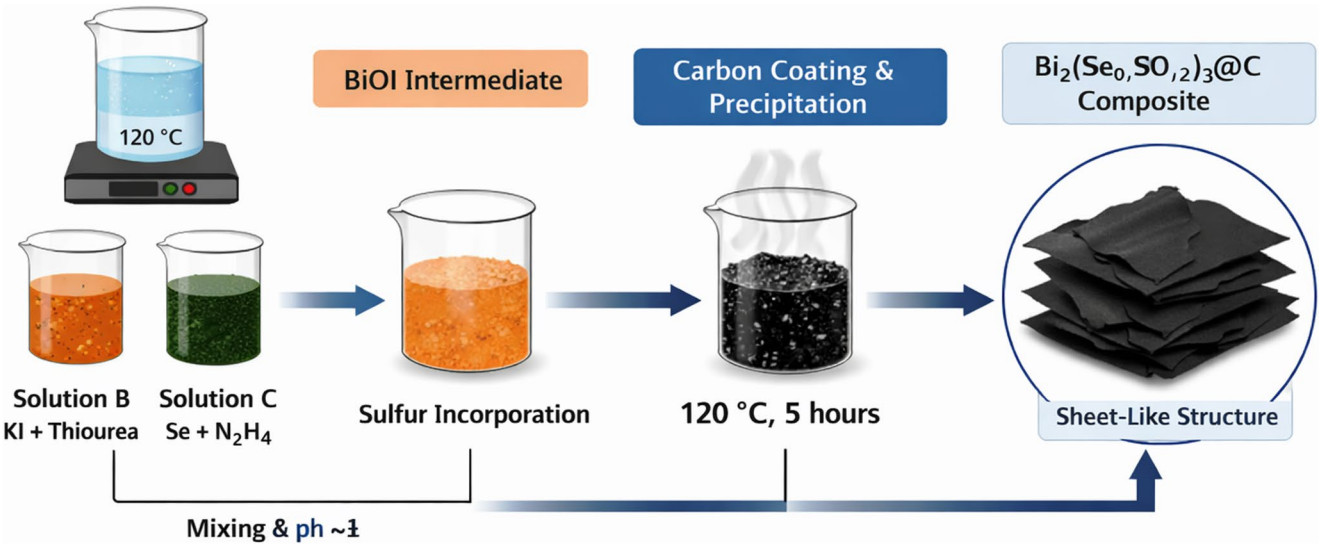

Fig. 1 Graphical illustration of the synthesis process of i2(Se0.8S0.2)3@C composites

3 Results and discussion

3.1 XRD analysis

The crystal structure of $Bi_2(Se_{0.8}S_{0.2})_3$@C material was determined by X-ray diffraction analysis. The pattern is seen in Fig. 2. The standard pattern (JCPDS No. 33–0214) indicates that all the reflections belong to the rhombohedral phase of Bi_2Se_3. The primary diffraction peaks are observed at 2θ values of 18.5°, 27.8°, 34.9°, 47.1°, 52.4°, 56.2°, and 65.4° which match to the planes (006), (101), (109), (118), (110), (015), and (205), respectively. No other reflections corresponding to unreacted elements or other phases like Bi_2S_3 were detected, indicating the exceptional purity of the composite sample. No peaks of sulfur phases are observed in the solid solution which shows uniform distribution of sulfur ions over Se^{2-} sites. In addition, due to the amorphous nature, there is no carbon in the pattern. Table 1 shows the structural properties.

3.2 TGA analysis

As illustrated by TGA analysis curve (Figure S1), the composite $Bi_2(Se_{0.8}S_{0.2})_3$@C displays only slight weight loss below 150 °C following the removal of surface-adsorbed water and residual solvents. Between 200 and 400 °C a large loss in mass occurs due to the loss of carbon and the remaining organic species. As the temperature rises, the curve gets more stable, indicating that the material has perfect stability.

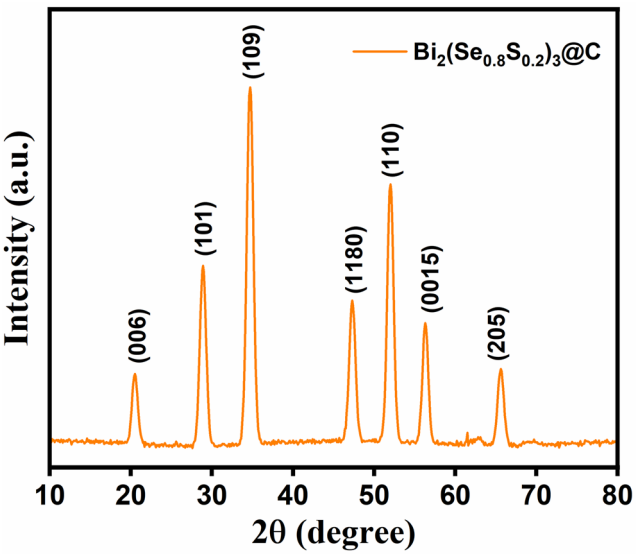

Fig. 2 XRD pattern of $Bi_2(Se_{0.8}S_{0.2})$@C

3.3 Morphological analysis

SEM and TEM images of the $Bi_2(Se_{0.8}S_{0.2})_3$@C composite samples are shown in Fig. 3(a-f). SEM scans at different magnifications confirm that the material has a porous structure with randomly dispersed interconnecting layers of nanosheets (Fig. 3a–c). Nanosheets are 2D structures with a thickness of 20–40 nm and lateral dimensions of 200–500 nm. This arrangement is helpful for electrochemical systems, by increasing the available surface area and allowing electrolyte ions to penetrate into the porous matrix. Figure 3d is a transmission electron micrograph showing other microstructural characteristics, including a carbonaceous matrices with thin, slightly bent nanosheets. The carbon part is tightly bound to the $Bi_2(Se_0.8\ S_0.2)_3$ domains and the overlapping sheets can build a conductive network. This network can help to transport the charges and electrons in the electrochemical reactions.

Identification of these constituents confirms efficient incorporation of sulfur into the bismuth selenide matrix with retention of the carbon framework. Importantly, no further peaks corresponding to other impurity elements were seen, indicating the exceptional purity of the synthesized composite. The particle size distribution seen in Fig. 3e suggests that the nanosheets consist of nanocrystalline particles with an average size of about 20 nm. The incorporation of these nanoscale building units into the layered architecture leads to an increase in density of electrochemically active sites. This nanoscale feature, together with the porous and sheet-like structure, can improve the ion accessibility and charge storage capacity, therefore improving the overall electrochemical properties of the $Bi_2(Se_{0.8}S_{0.2})_3$@C electrode material.

3.4 Elemental composition analysis

Figure 4 depicts the distribution of elements in the $Bi_2(Se_{0.6}S_{0.2})_3$@C sample. The homogeneous distribution of Bi, Se, and S throughout the structure suggests no apparent separated phases. The overlapping of Se and S signals shows that sulphur is not a separate phase but a structural component of the lattice. The uniform distribution of the carbon signal in the material is another feature of a continuous amorphous coating. There is a high compositional

Table 1 Physical Parameters Derived from XRD

Parameter	Symbol	Value
Crystal system	-	Rhombohedral
Space group	-	*R*–3*m*
Lattice parameter	*a* (Å) and *c* (Å)	~4.12–4.14
Unit cell volume	*V* (Å³)	~28.5–28.7
Crystallite size	*D (nm)*	~420–425~15–30
Microstrain	ε	~10^{-3}
Dislocation density	δ (nm^{-2})	~10^{-3}–10^{-2}

homogeneity since there are no places with centered components.

3.5 N_2 adsorption desorption analysis

The distribution of pore diameters is shown in Figure S2 and the N_2 adsorption-desorption isotherm of the $Bi_2(Se_{0.8}S_{0.2})_3$@C sample is shown in Figure S3. The adsorption curve is of type IV with a prominent H3 hysteresis loop, demonstrating the presence of mesopores arising from disordered sheet-like structures. The porosity is clearly visible with a specific surface area of about 145 m^2g^{-1}. As can be seen from the pore size distribution, the pores are definitely mesoporous with an average pore width of about 6.7 nm. This structure increases electrochemical performance by permitting the electrolyte ions to access the inside of the material.

3.6 XPS analysis

The XPS analysis results for the $Bi_2(Se_{0.8}S_{0.2})_3$@C sample are presented in Fig. 5. The survey scan confirms the lack of pollutants and shows only Bi, Se and C are present. The high resolution spectra of the Bi 4f area has two peaks at 159.1 eV and 164.4 eV representing the Bi $4f_{7/2}$ and Bi $4f_{5/2}$, respectively, showing the presence of bismuth in +3 oxidation state. The Se 3d spectra shows peaks at 54.6 eV and 58.5 eV corresponding to the Se $3d_{5/2}$ and Se $3d_{3/2}$, respectively, which confirms the presence of selenium in the reduced Se^{2-} form in the lattice [24]. The C 1s peak at 283.8 eV is related to graphitic carbon, indicating the presence of conductive carbon layer [25]. These results confirm the successful fabrication of the composite where the carbon phase enables charge transfer and the chalcogenide structure acts as active sites for electrochemical processes.

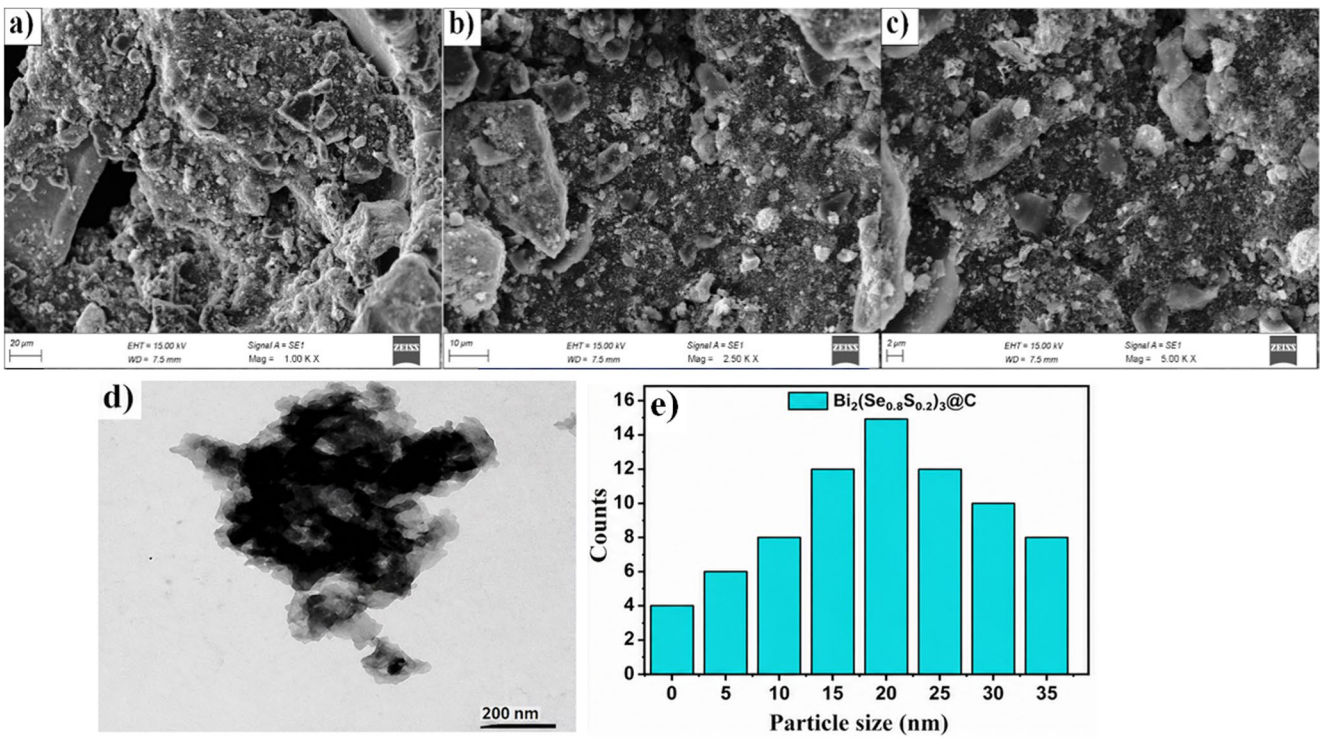

Fig. 3 (**a**-**c**) SEM images of $Bi_2(Se_{0.8}S_{0.2})_3$@C with different magnifications, **d**) TEM image of $Bi_2(Se_{0.8}S_{0.2})_3$@C, **e**) Particle size curve of $Bi_2(Se_{0.8}S_{0.2})_3$@C

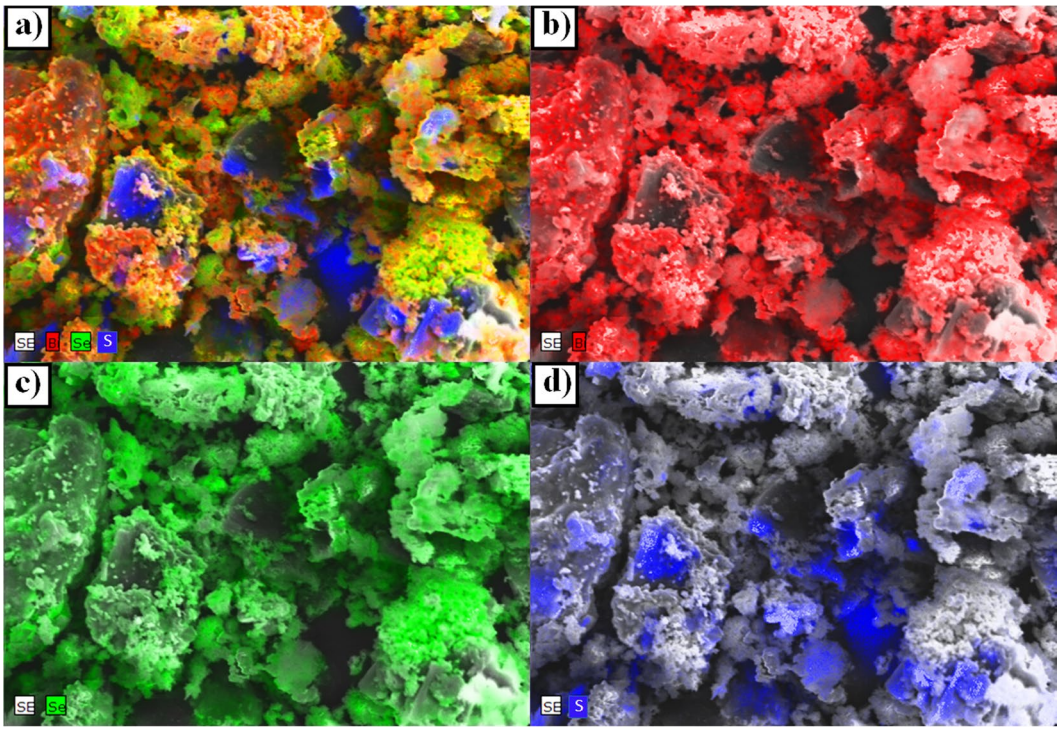

Fig. 4 Elemental mapping images of the $Bi_2(Se_{0.8}S_{0.2})_3$@C composite (**a**) survey, (**b**) Bi, (**c**) Se, (**d**) S

3.7 Electrochemical analysis

3.7.1 Three electrode system

The electrochemical properties of $Bi_2(Se_{0.8}S_{0.2})_3$@C electrode were measured by CV and shown in Fig. 6. Figure 6a shows the operating three-electrode testing equipment and the steps for functional electrode fabrication and preparation for electrochemical measurements [26–28]. Figure 6b shows the CV curves of the $Bi_2(Se_{0.8}S_{0.2})_3$@C electrode at different scan rates. These approximately rectangular curves do not have clear redox peaks, indicating that the charge storage mechanism tends to dominate by electric double-layer capacitance (EDLC) and not faradaic processes [29]. The rectangular profile is maintained at high scan rates, indicative of the good electrochemical reversal and quick ion transport of the electrode architecture.

The charge storage kinetics were studied by applying the power-law equation ($i = av^b$) to investigate the correlation between the scan rate and the peak current. Figure 6c shows that the calculated b value was 0.85. The b value indicates that the charge storage process is mostly governed by surface capacitive processes rather than diffusion-controlled mechanisms [30–32]. Figure 6d shows the quantitative difference between diffusion and the capacitive contribution. The data (Fig. 6d) reveal that at a scan rate of 10 mVs^{-1}, a surface-controlled capacitance accounts for ~63% of the overall charge storage behaviour, increasing to nearly 93% at 100 mVs^{-1}. The charge accumulation in the electrode is mainly due to fast surface reactions and the formation of an electric double layer, as the surface capacitive contribution increases dramatically at higher scan rates. This indicates the synergistic effect of the porous nanosheet building and conductive carbon network design that facilitates quick ion adsorption and efficient electron transport. Overall, our findings confirm the excellent surface-dominated capacitive properties of the $Bi_2(Se_{0.8}S_{0.2})_3$@C electrode, which is promising for high-rate electrochemical energy storage performance [33, 34]. The CV curve is separated using the Dunn approach as shown in Fig. 6(e). The shaded area represents the capacitive (surface-controlled) contribution and the unshaded area is related to the diffusion-controlled process. The

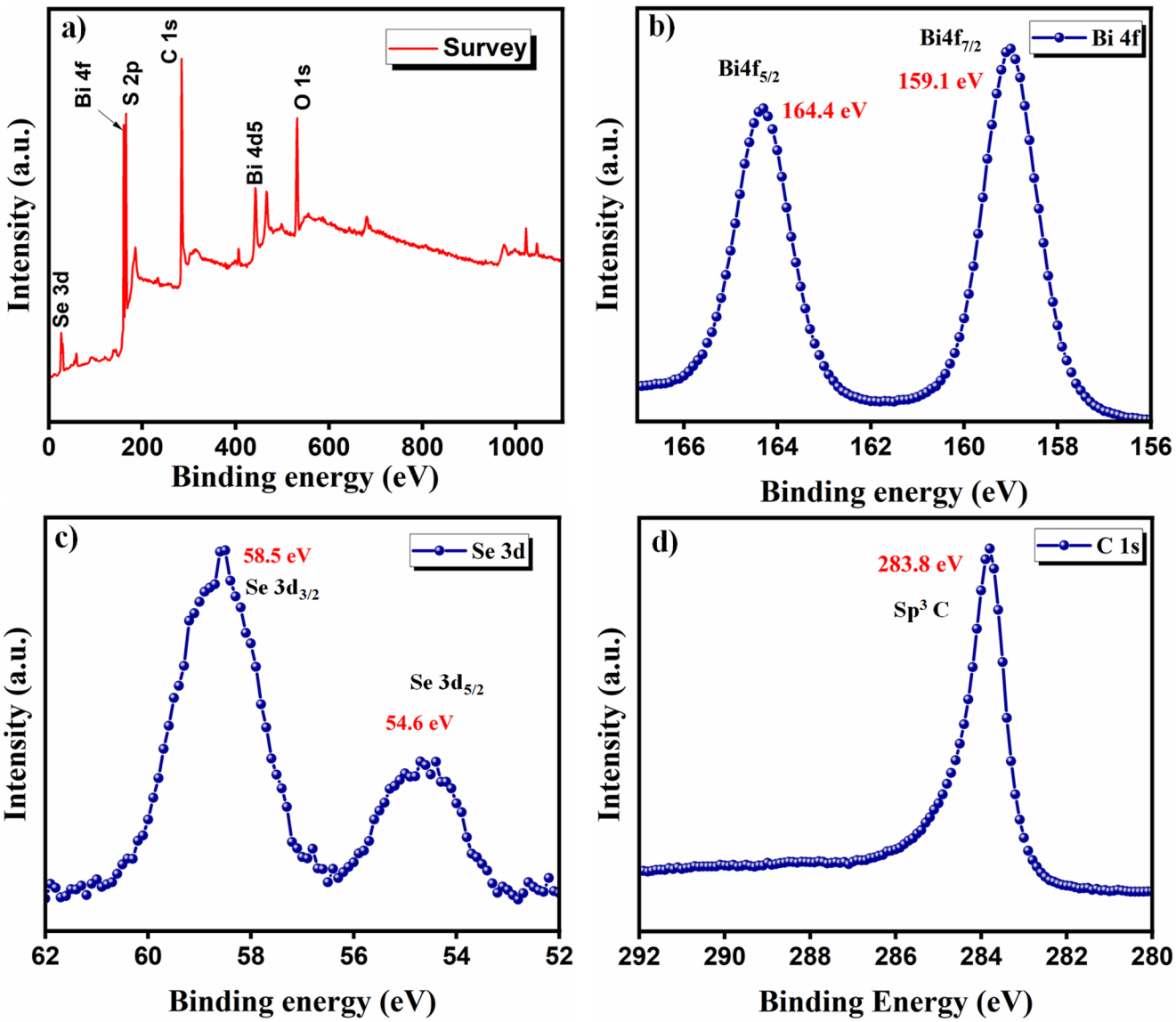

Fig. 5 XPS of $Bi_2(Se_{0.8}S_{0.2})_3$@C, (**a**) aurvey, (**b**) Bi 4f, (**c**) Se 3d, (**d**) C 1s

surface-controlled charge storage contributes > 93% to the total at scan rates of 10 and 100 mV s^{-1}, while the contribution from diffusion decreases with increasing scan rate. This behaviour indicates that the nanosheet geometry and conductive carbon layer, which provide ion accessibility and electron mobility, enable the electrode to store charge predominantly via fast surface reactions. Electrochemical impedance behavior, rate capability, cycle stability, and GCD features of $Bi_2(Se_{0.8}S_{0.2})_3$ and $Bi_2(Se_{0.8}S_{0.2})_3$@C electrodes in 3 M KOH electrolyte are shown in Fig. 7. Figure 7a and b show the GCD curves. Moreover, $Bi_2(Se_{0.8}S_{0.2})_3$@C composite demonstrates higher charge storage capacity compared to the pure $Bi_2(Se_{0.8}S_{0.2})_3$@C electrode with much longer discharge times. This boost is ascribed to the introduction of the carbon framework thereby boosting the electrical conductivity and helps the effective electron transport in the electrode. The CV patterns and a b-value of 0.85 show that the charge storage is mostly controlled by fast processes at or near the electrode surface. The presence of minor plateau in the GCD curves could be an indication of fast and reversible redox processes occurring in the electrode material. Such properties are typical of pseudocapacitive systems where surface adsorption and restricted ion transport are involved. Previous studies [35, 36] suggest that the electrode is mainly pseudocapacitive in nature with a minor contribution from the battery type activities. The Cs value was calculated with an integral-based technique to improve the accuracy. This allowed the required capacitance to be re-calculated by using the given formula.

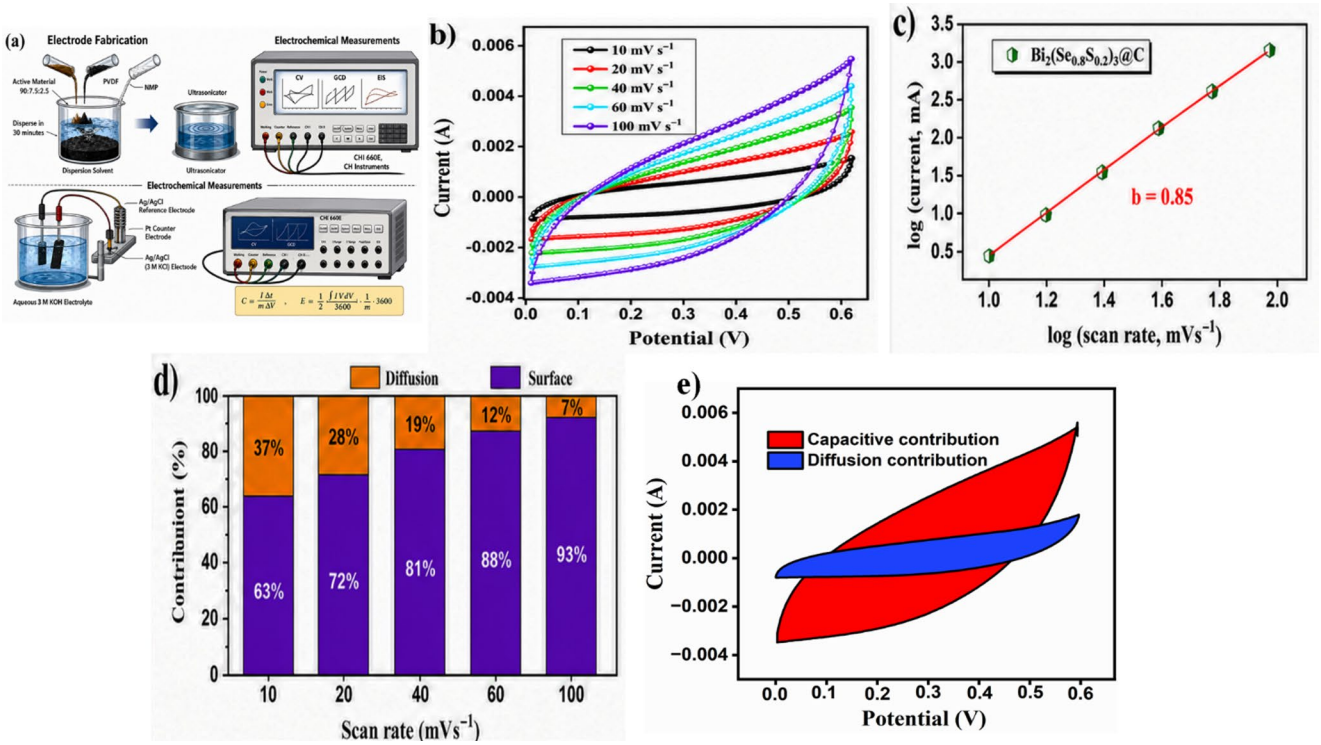

Fig. 6 (**a**) A schematic depiction of the electrode preparation and the electrochemical setup, (**b**) CV curves of $Bi_2(Se_{0.8}S_{0.2})_3$@C at different scan rates, (**c**) A plot of Log(i) against log(v) derived from cyclic voltammetry data of the $Bi_2(Se_{0.8}S_{0.2})_3$@C electrode to determine the b value, (**d**) A bar diagram showing the Surface-Diffusion contribution, (**e**) A color-shaded CV curve of $Bi_2(Se_{0.8}S_{0.2})_3$@C illustrating capacitive (shaded) and diffusion-controlled contributions using the Dunn method

$$C = 1m\triangle V \int I\, dt \tag{1}$$

where ΔV stands for the potential window and m for the mass of the active material [37]. The specific capacitance values calculated from GCD measurements at different current densities are shown in Fig. 7c. While the pristine $Bi_2(Se_{0.8}S_{0.2})$ electrode shows lower capacitance values of 495, 433, 345, 288 and 169 F g^{-1} at the same testing conditions. The $Bi_2(Se_{0.8}S_{0.2})_3$@C electrode achieves higher specific capacitance of 950, 856, 701, 622 and 501 F g^{-1} at current densities of 1, 2, 3, 4 and 5 A g^{-1}, respectively. The significant enhancement of the electrochemical characteristics of the $Bi_2(Se_{0.8}S_{0.2})_3$@C electrode is attributed to the combined effects of the S/Se solid-solution lattice and the conductive amorphous carbon matrices. This synergistic aggregation benefits the ion transport at electrode-electrolyte interface and accelerates the charge transfer. The findings of additional charge-discharge experiments to evaluate the long-term cycling stability of the electrodes are shown in Fig. 7d and e.

After long-time cycling, the pure $Bi_2(Se_{0.8}S_{0.2})_3$electrode retains around 75% of its initial capacitance, whereas the $Bi_2(Se_{0.8}S_{0.2})_3$@C composite exhibits outstanding structural integrity with retention of more than 98% of its original capacitance. The carbon matrix may effectively inhibit the structural degradation and maintain the electrode integrity during the continuous electrochemical cycling process, thereby improving the stability of the composite electrode. The Nyquist plot and equivalent circuit of the samples are shown in Fig. 7(f) and inset. In the high frequency domain of the Nyquist spectra, a semicircular arc corresponding to the charge transfer process is observed, while an inclined straight line corresponding to the ion diffusion behaviour is observed in the low frequency domain. The semicircle of $Bi_2(Se_{0.8}S_{0.2})_3$@C composite is much smaller, which indicates the improved electrical conductivity and the faster pathways of electron transport due to the conductive carbon layer. On the other hand, the pristine $Bi_2(Se_{0.8}S_{0.2})_3$ electrode shows a relatively larger semicircle indicating a higher interfacial resistance. The equivalent circuit fitting shows that $Bi_2(Se_{0.8}S_{0.2})_3$@C electrode has less resistances

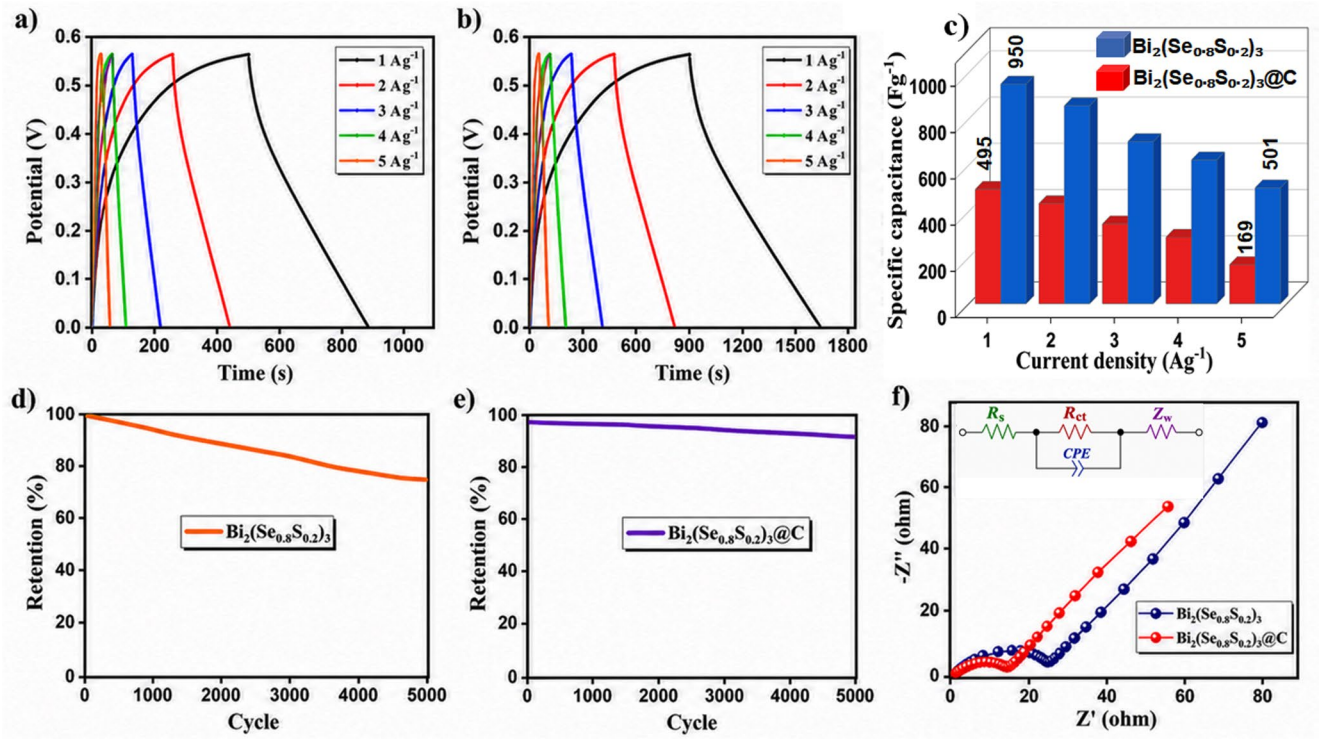

Fig. 7 GCD profile of (**a**) $Bi_2(Se_{0.8}S_{0.2})_3$. (**b**) $Bi_2(Se_{0.8}S_{0.2})_3$@C, (**c**) Specific capacitances as a function of current density, Retention curve of (**d**) $Bi_2(Se_{0.8}S_{0.2})_3$, (**e**) $Bi_2(Se_{0.8}S_{0.2})_3$@C, (**f**) Nyquist plot of $Bi_2(Se_{0.8}S_{0.2})_3$ and $Bi_2(Se_{0.8}S_{0.2})_3$@C with equivalent circuit (inset)

(Rs = 0.84 Ω and Rct = 2.13 Ω) compared to $Bi_2(Se_{0.8}S_{0.2})$ electrode with Rs ≈ 1.21 Ω and Rct ≈ 4.86 Ω. The composite electrode shows improved capacitive performance with a CPE value of 5.8×10^{-4} F as compared to 3.2×10^{-4} F of $Bi_2(Se_{0.6}S_{0.2})$ suggesting a more favorable non-ideal capacitive response of the electrode surface. The Warburg impedance (ZW = 0.92 Ω $s^{-1/2}$) of the carbon-modified electrode was lower than that of the virgin material (1.67 Ω $s^{-1/2}$), suggesting that the improved ion transport channels are available in the electrolyte.The use of carbon significantly enhances electrical conductivity and electrochemical reaction kinetics, which facilitates a faster ion transport and improved electrochemical performance of the $Bi_2(Se_{0.8}S_{0.2})_3$@C electrode. It indicates lower charge transfer resistance and lower diffusion impedance. Table 2 further shows that the efficiency obtained in this work is better than the ones shown in earlier research [38–43].

3.7.2 Two electrode system

The asymmetric supercapacitor (ASC) device was produced with activated carbon (AC) as a negative electrode and $Bi_2(Se_{0.8}S_{0.2})_3$@C as a positive electrode with alkaline KOH as an electrolyte (Fig. 8). Figure 8a depicts the architecture of the ASC system where the two-electrode energy storage setup, the AC anode, the $Bi_2(Se_{0.8}S_{0.2})_3$@C cathode, the electrolyte medium, and the separator are clearly visible. The approximately rectangular cyclic voltammetry curves obtained at different scan rates (Fig. 8b) suggest that the charge storage of the device is mostly dominated by the EDLC behavior of the porous AC electrode. The data suggest that the $Bi_2(Se_{0.8}S_{0.2})_3$@C electrode can give extra surface redox activity. The CV curves at different scan rates are similar, indicating the high electrochemical reversibility at electrode-electrolyte interface, quick surface reactions and efficient ion transport. entering the active zones further within the electrode during rapid charge-discharge cycles. Further confirmation of the electrochemical behavior of activated carbon is obtained from CV, GCD and EIS studies (Figures S4– S6). The absence of distinguishable peaks in the CV curves obtained in the potential window from −1.0 to 0.0 V (Fig. 8b) indicates that electrostatic ion adsorption is the main charge storage process, as the curves present a rectangular shape. The charge-discharge curves are symmetrical and relatively linear, indicating stable and reversible cycle behaviour. The slope observed in the low-frequency region and the small intercept in the high-frequency region on the impedance plot are indicative of low resistance and

Table 2 Electrochemical comparison performance

Electrode	Electrolyte	Specific capacitance (Fg^{-1})	Retention (%)/ cycles	Ref.
Bi_2S_3	1 M KOH	748	92.5/5000	[38]
Bi_2S_3/Se	1 M Na_2SO_4	647	90/3000	[39]
Bi_2Se_3	1 M KOH	274	85.5/5000	[40]
Bi_2Se_3	1 M KOH	662	95/5000	[41]
Bi_2S_3	3 M KOH	1015	93/10,000	[42]
Bi_2Se_3@C	1 M KOH	569	90.5/3000	[43]
$Bi_2(Se_{0.8}S_{0.2})_3$@C	3 M KOH	1098	98/5000	This work

efficient ion conduction. These results confirm that the material behaves predominantly as an electric double-layer capacitor in the whole investigated potential range. The GCD curves at different current densities (Fig. 8c) present symmetric triangular forms with a slight decrease in voltage in the interior, which confirm the strong capacitive nature and high charge–discharge reversibility. Figure 8d shows the discharge profiles, where the specific capacitance values are ~161, 72, 64, 50 and 28 F g^{-1} for current densities of 1, 2, 3, 4 and 5 A g^{-1}, respectively. The large drop in capacitance at high current density is ascribed to restricted penetration of electrolyte ions. The coulombic efficiency and cycle stability of the ASC device are shown in Fig. 8e. The device exhibits about 98.2% capacitance retention over long-term charge-discharge cycles, indicating the excellent structural stability and electrochemical stability of the electrode materials. Besides, the coulombic efficiency is about 102.3% that clearly indicates highly reversible charge storage mechanisms with minor energy loss even after several cycles. The fitted equivalent circuit is shown in Fig. 8(f) together with the Nyquist plot of the finished ASC device. The figure illustrates charge transfer and ion diffusion processes as a straight line at low frequencies and a little arc in the high frequency range. The actual axis intercept is about 0.72 Ω which indicates low internal resistance and this is the solution resistance (Rs). The semicircle reveals a charge transfer resistance (Rct) of about 1.85 Ω, indicating the interfacial processes are fast. The Warburg component (Z_v) is about 0.65 Ω s1/2, indicating a steady ion flow. However, the CPE value is 6.1×10^{-4} F, which is adequate for the capacitive behavior. The device's diffusion properties and low resistance show efficient electrochemical performance. The Ragone plot of the fabricated asymmetric supercapacitor device $Bi_2(Se_{0.8}S_{0.2})_3$@C//AC is shown in Fig. 9. The graph displays the relation between the power density and the energy density and gives essential information about the capability of energy storage of the device. The device has a current density of 1 A g^{-1}, an energy density of 65 Wh kg^{-1} and a power density of 877 W kg^{-1}, indicating a promising future for efficient energy storage and distribution. The device exhibits excellent rate performance and fast electrochemical reactivity with a remarkable energy

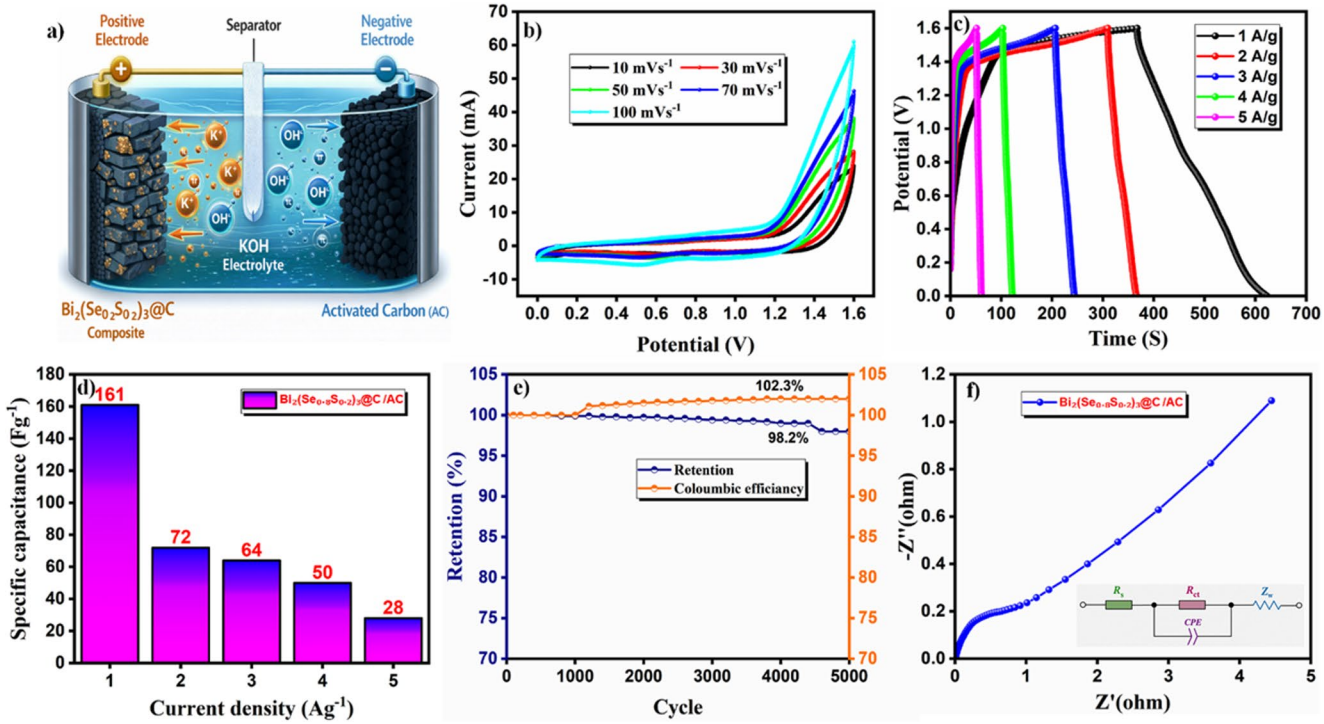

Fig. 8 Graphical illustration of fabricated ASC ($Bi_2(Se_{0.8}S_{0.2})_3$@C as positive and AC as negative), (**b**) CV curves of ASC with various scan rates, (**c**) GCD profile of ASC with various current density, (**d**) cs values with respect to current density, (**e**) retention and coulombic efficiency plot of ASC, (**f**) Nyquist plot of ASC

density of 35 Wh kg^{-1} and power density of 3117 W kg^{-1} at a current density of 5 A g^{-1}.

These values surpass those documented in other studies, including Bi_2S_3 and Ce doped Co_3O_4 (498.9 W Kg^{-1} and 0.5 Wh kg^{-1}) [44], Bi_2Se_3//$NiCo_2S_4$ (800 W Kg^{-1} and 48 Wh kg^{-1}) [45], ZnS/Bi_2Se_3 (4990 W Kg^{-1} and 56 Wh kg^{-1}) [46], Ni-Co-Mn phosphate@$Ti_3C_2T_x$ (800 W Kg^{-1} and 22 Wh kg^{-1}) [47], and $Co_xMn_{3-x}(PO_4)_2 \cdot nH_2O$ (790 W Kg^{-1}). Figure S7 TEM picture of $Bi_2(Se_{0.8}S_{0.2})_3$@C following electrochemical cycling. Moreover, the material maintains its laminar structure after prolonged use, with a network of interconnected and consistently distributed thin layers. The absence of major cracking or dense aggregation in the structure under cycling conditions is encouraging. This structure, conserved with such care, allows ions to move smoothly and efficiently, and so improves the transfer of charge. The carbon phase enhances structural integrity by enhancing resistance to operating forces. The material is stable in the form of nanosheets, making it suitable for supercapacitor applications and providing continuous performance [48].

Figure 10 shows the working of the fabricated asymmetric supercapacitor (ASC) device consisting of two coin-type cells in series. With this configuration the device is able to power LEDs. The energy conserved for a just 20 s of charging is enough to light up multicoloured LEDs for a long time. Figures 9b–d demonstrate the energy storage and transfer to blue, violet and orange LEDs by the ASC device, rendering light visible for approximately 10 min. These LEDs work well, proving that the system is able to produce a suitable voltage with two batteries in series. Violet, blue and orange LEDs required voltages of 3.1 to 3.4, 2.8 to 3.2 and 2.0 to 2.2, respectively. This shows that the ASC device is capable of powering tiny LEDs and controlling small electrical components. $Bi_2(Se_{0.8}S_{0.2})_3$@C//AC asymmetric supercapacitors can achieve efficient energy storage, stable discharge and long-term lighting under fast charge. The arrangements indicate the possibilities of the energy storage device for portable gadgets and compact power supplies [49].

3.8 MB photocatalytic test

The photocatalytic activity of the produced compounds was measured by the degradation of methylene blue (MB) dye under visible light. Common visible light sources were a 300 W xenon or halogen lamp with a UV cutoff filter (λ>420 nm). The concentration of the MB dye solution ranged between 5 and 20 mgL^{-1}. 10 mgL^{-1} was the most common concentration for routine tests. Add 0.5–1.0 g L^{-1} (50 mg per 100 mL) of the photocatalyst in the dye solution and stir regularly. Before light irradiation, the catalyst surface and dye molecules were mixed by a magnetic stirrer for 30 min to reach adsorption–desorption equilibrium. Degradation was induced by light irradiation and dye concentrations were determined by UV–Vis absorption spectroscopy. Figure S8. UV–vis absorption spectra of MB in the presence

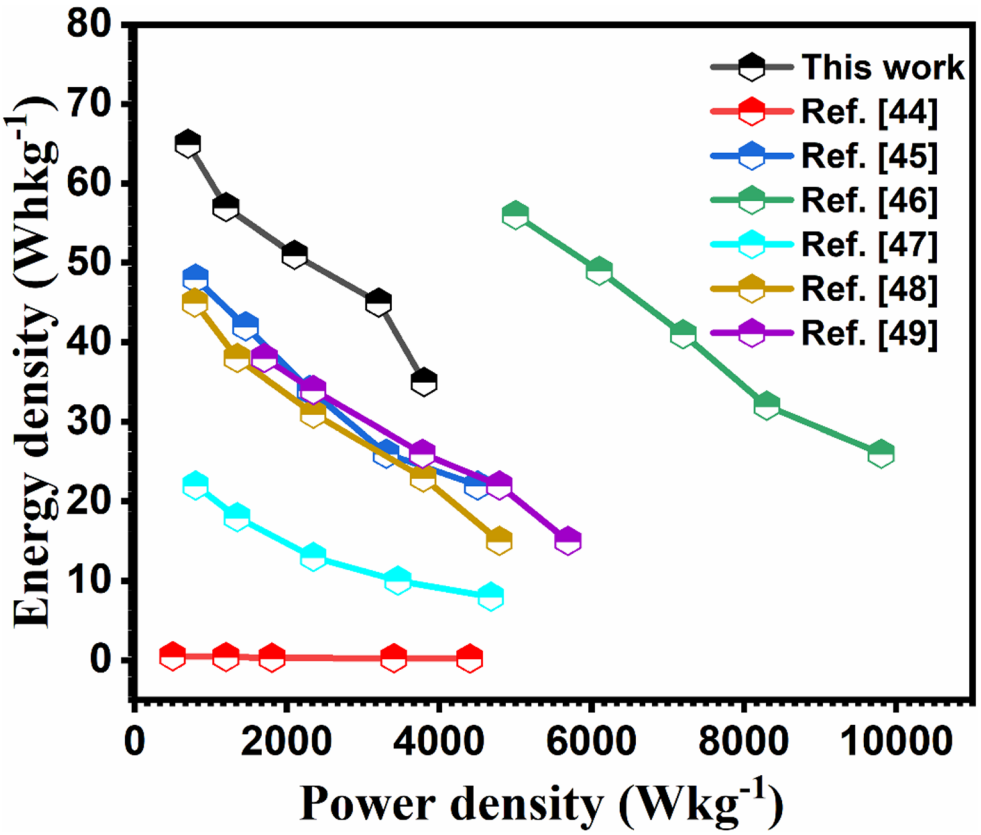

Fig. 9 Ragone plot of the ASC device with comparsion performance

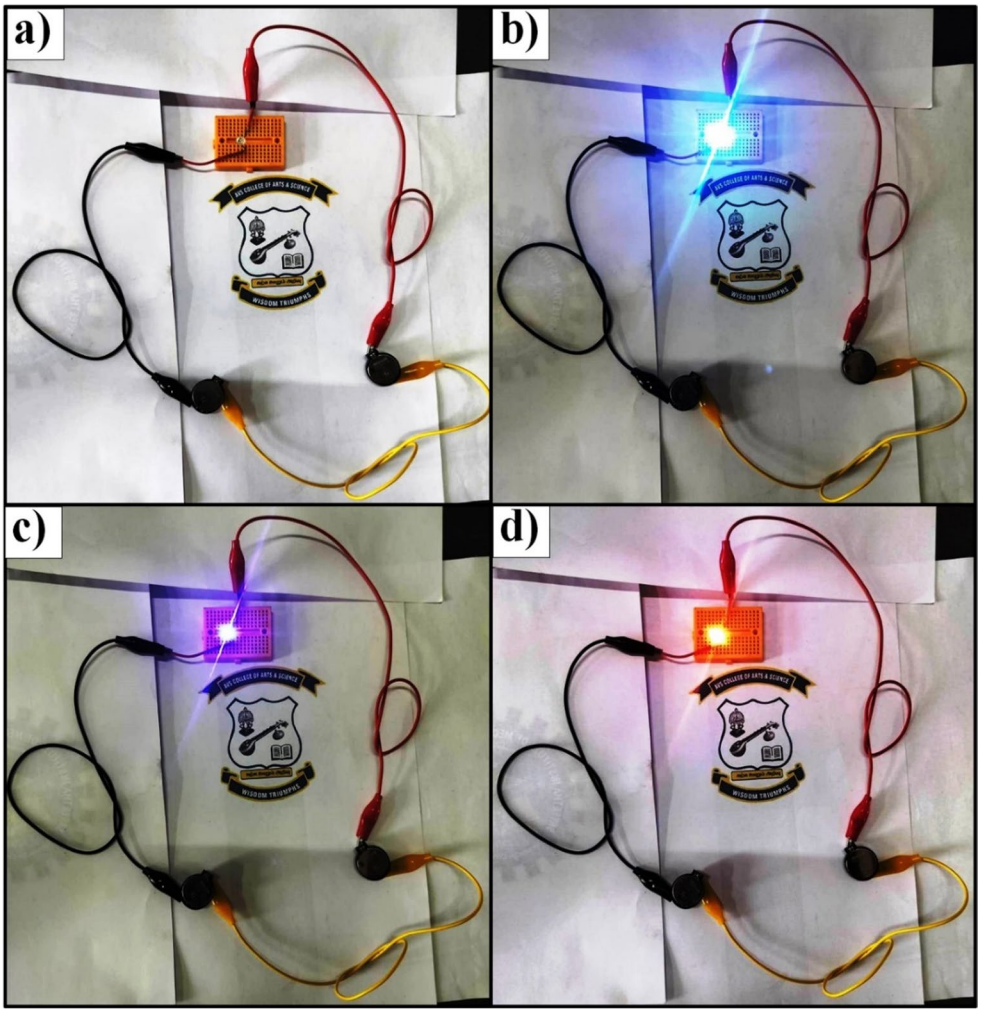

Fig. 10 Practical demonstration of the fabricated asymmetric supercapacitor device. (**a**) Photograph of two coin-type $Bi_2(Se_{0.8}S_{0.2})_3$@C//AC ASC cells connected in series, (**b**) blue LED illumination, (**c**) violet LED illumination, and (**d**) orange LED illumination powered by the charged device. The LEDs remain lit for nearly 10 min after a short charging period of approximately 20 s, confirming the efficient energy storage and power delivery capability of the ASC system.

of $Bi_2(Se_{0.8}S_{0.2})_3$@C. The lowering of the magnitude of the characteristic absorption peak signifies slow dye degradation. The photocatalytic activity of $Bi_2(Se_{0.8}S_{0.2})_3$@C composite is substantially higher than that of pure $Bi_2(Se_{0.8}S_{0.2})$, as seen by the time degradation curve in Fig. S9. Under the same conditions, the degrading efficiency of $Bi_2(Se_{0.8}S_{0.2})_3$@C is about 92%, but the degrading efficiency of $Bi_2(Se_{0.8}S_{0.2})_3$ is only 56%. The performance enhancement is ascribed to the use of sulphur in the conductive carbon matrix that reduces electron-hole recombination and promotes effective charge separation. The results of further investigation of the reaction kinetics with a pseudo-first-order model are shown in Figure S10. The degradation rate constants of $Bi_2(Se_{0.8}S_{0.2})_3$@C and $Bi_2(Se_{0.8}S_{0.2})_3$@C are 0.0045 min^{-1} and 0.0761 min^{-1} respectively. The enhancement of the kinetic performances is mainly attributed to the enhancements of the carbon network in the electron transport channels and the expansion of the accessible active sites for the photocatalytic processes. Long-term stability and reusability of the $Bi_2(Se_{0.8}S_{0.2})_3$@C photocatalyst were tested for five cycles, as shown in Figure S11. The composite is remarkably stable, losing only 2.5% of its original efficiency after five cycles. Over time, this minor degradation shows the material has outstanding resistance to photocorrosion and structural stability.

4 Conclsuion

In brief, a composite material of sulphur-modified bismuth selenide and carbon, denoted as $Bi_2(Se_{0.8}S_{0.2})_3$@C, was effectively prepared using a facile chemical precipitation method. The material exhibited good electrochemical performance in supercapacitor tests. The morphological study showed the presence of nanosheet-like structures uniformly scattered in a conductive carbon matrix. The structural study confirmed the creation of a bismuth selenosulfide solid-solution structure. The network structure provides a rapid electron transfer in electrochemical process and a high number of electroactive sites. The $Bi_2(Se_{0.8}S_{0.2})_3$@C electrode delivered a

specific capacitance of 950 Fg^{-1} at 1 Ag^{-1}, and exhibited excellent cycling stability, keeping over 98% of its initial capacitance after 5000 charge-discharge cycles. An asymmetric supercapacitor with activated carbon as a negative electrode and $Bi_2(Se_{0.8}S_{0.2})_3$@C as a positive electrode showed a good energy density of 65 $Whkg^{-1}$ at a power density of 877 W kg^{-1} and 35 $Whkg^{-1}$ at 3117 W kg^{-1}, demonstrating a good compromise between energy and power density. Also, the practicality and fast energy storage capabilities of the system was shown by driving many LEDs for around 10 min by two connected in series coin-type ASC devices after about 20 s of charging. Furthermore, $Bi_2(Se_{0.8}S_{0.2})_3$@C showed excellent photocatalytic performance with the degradation of MB approximately 92%, higher rate constant (0.0761 min^{-1}) and good stability for five cycles due to the higher charge separation. The results indicate that the incorporation of sulphur into the bismuth selenide framework, along with the addition of conductive carbon, boosts the electrochemical activity and charge-transfer kinetics.

Supplementary Information The online version contains supplementary material available at https://doi.org/10.1007/s10934-026-01933-y.

Author contributions **A. Parveen: ** Conceptualization, methodology design, experimental investigation, data analysis, and preparation of the original manuscript draft.**N. Surumbarkuzhali: ** Supervision, project administration, validation of results, and critical revision of the manuscript.**D. Anitha Kumari: ** Data curation, statistical analysis, and literature review.**R. Kanimozhi: ** Material synthesis assistance, characterization, and interpretation of results.**Arumugam Krishnan Arulmozhi: ** Theoretical modeling, data visualization, and proofreading of the final manuscript.

Funding The authors did not receive any specific grant from funding agencies in the public, commercial, or not-for-profit sectors.

Data availability The data that support the findings of this study are available from the corresponding author upon reasonable request.

Declarations

Ethical Approval This article does not contain any studies involving human participants or animals performed by any of the authors.

Competing interests The authors declare no competing interests.

References

1. K. Dissanayake, D.K. Abeywardana, A review of supercapacitors: Materials, technology, challenges, and renewable energy applications. J. Energy Storage. **96**, 112563 (2024)
2. N. Singh, V. Singh, N. Bisht, P. Negi, A. Dhyani, R.K. Sharma, B.S. Tewari, A comprehensive review on supercapacitors: Basics to recent advancements. J. Energy Storage. **121**, 116498 (2025)
3. C.V.V. Muralee Gopi, S. Alzahmi, V. Narayanaswamy, R. Vinodh, B. Issa, I.M. Obaidat, Supercapacitors: A promising solution for sustainable energy storage and diverse applications, Journal of Energy Storage 114 (2025) 115729
4. A. Bidhan Pandit, C. Varez, Huang, Polymer electrodes in solid-state metal-ion batteries: An in-depth review on recent advances, challenges, and future prospects. eScience Energy. **2**, 100033 (2026)
5. M. Bidhan Pandit, B.P. Johansen, S. Andersen, Cynthia, B. Martínez-Cisneros, D.B. Levenfeld, Ravnsbæk, Alejandro Varez, All-solid-state sodium-ion batteries operating at room temperature based on NASICON-type $NaTi_2(PO_4)_3$ cathode and ceramic NASICON solid electrolyte: A complete in situ synchrotron X-ray study. Chem. Eng. J. **472**, 144509 (2023)
6. M. Bidhan Pandit, C.S. Johansen, J.M. Martínez-Cisneros, B. Naranjo-Balseca, D.B. Levenfeld, A. Ravnsbæk, Varez, $Na_3V_2(PO_4)_3$ Cathode for Room-Temperature Solid-State Sodium-Ion Batteries: Advanced In Situ Synchrotron X-ray Studies to Understand Intermediate Phase Evolution. Chem. Mater. **36**, 2314–2324 (2024)
7. S.R. Bidhan Pandit, Y. Rondiya, Nelson, F. Dzade, Shoyebmohamad, N. Shaikh, E.S. Kumar, A.A. Goda, R.S. Al-Kahtani, S. Mane, R.R. Mathur, Salunkhe, High Stability and Long Cycle Life of Rechargeable Sodium-Ion Battery Using Manganese Oxide Cathode: A Combined Density Functional Theory (DFT) and Experimental Study, ACS Appl. Mater. Interfaces. **13**, 11433–11441 (2021)
8. C. Subashini, R. Sivasubramanian, M.M. Sundaram, N. Priyadharsini, The evolution of allotropic forms of $Na_2CoP_2O_7$ electrode and its role in future hybrid energy storage. J. Energy Storage. **130**, 117390 (2025)
9. Y. Hao, H. Guo, H. Ren, Z. Yang, L. Peng, Y. Liu, W. Yang, Highly dispersive nickel vanadium oxide nanoparticles anchored on nickel cobalt phosphate micron-sheets as cathodes for high-energy hybrid supercapacitor devices. J. Alloy Compd. **1010**, 177893 (2025)
10. M. Saqib, A. Asghar, Z. Chen, A.A.A. Hafez, M.Y. Almashnowi, Q. Arshad, M.Y. Awaji, Y. Javad, M. Kuku, M.S. Rashid, Fabrication of asymmetric supercapattery with faradaic and non-faradaic quantification by $Co_3(PO_4)_2$/GO composite as a positive electrode. J. Alloy Compd. **1010**, 177986 (2025)
11. J. Kim, S. Song, C.S. Lee, M. Lee, J. Bae, Prominent enhancement of stability under high current density of $LiFePO_4$-based multidimensional nanocarbon composite as cathode for lithium-ion batteries. J. Colloid Interface Sci. **650**, 1958–1965 (2023)
12. S.M. Nikam, S.H. Sutar, A.I. Inamdar, S.H. Mujawar, Dendrite like nanorod bundles of cobalt phosphate electrodes for efficient water splitting and energy storage applications. J. Phys. Chem. Solids. **205**, 112808 (2025)
13. P. Bhanja, J. Na, T. Jing, J. Lin, T. Wakihara, A. Bhaumik, Y. Yamauchi, Nanoarchitectured metal phosphates and phosphonates: a new material horizon toward emerging applications. Chem. Mater. **31**, 5343–5362 (2019)
14. W. Tian, P. Ren, X. Hou, B. Fan, Y. Wang, L. Pei, H. Wang, Z. Chen, Y. Jin, Porous nickel–cobalt phosphate with oxygen-rich vacancies in situ grown on dopamine-modified cellulose textiles as self-supporting high mass loadings supercapacitor electrode. J. Colloid Interface Sci. **677**, 626–636 (2025)

15. S.S. Patil, S.B. Bhosale, S.S. Kumbhar, G.D. Jadhav, A. Ransing, V.G. Parale, H.-H. Park, C.D. Lokhande, U.M. Patil, Rational engineering of isostructural 1D cobalt hydroxide decorated 2D cobalt phosphate cathodes aided with isotype (pp) junctions for hybrid supercapacitors. J. Power Sources. **649**, 237461 (2025)
16. G. Xiao, H. Chen, S. Zhu, W. Zhao, S. Chen, Y. Wen, J. Chen, R. Ha, Y. Hao, J. Wang, Rational design of cobalt phosphide nanorods via hydrothermal-phosphorization for high-performance asymmetric supercapacitors. J. Alloy Compd. **1029**, 180758 (2025)
17. H. Chen, Y. Liao, Z. Ling, Z. Wu, A. Wen, M. Li et al., Accelerating multiple charge transport in topological insulator Bi_2Se_3 for high-performance cathode in aqueous zinc-ion battery. J. Energy Storage. **161**, 121968 (2026)
18. A. Qadir, M. Imran, R. Kousar, M.Z. Manzoor, M. Safdar et al., Two-dimensional Bi_2Se_3 and MoS_2 nanosheets as high-performance anode materials for supercapacitors. J. Power Sources. **666**, 239146 (2026)
19. D. Yulong Yang, Z. An, W. Si, W. Yang, L. Yue, X.-M. Shi, Zhang, Bottom-up design and efficient synthesis of layer-structured thermoelectric materials for power generation: the case of Bi_2Se_3, Vacuum. 247 (2026) 115149
20. B.M. Fominykh, A.N. Perevalova, V.Y. Irkhin, S.V. Naumov, K.V. Shalomov, N.V. Gushchina et al., Heavy ion irradiation-induced modifications in magnetotransport of the topological insulator Bi_2Se_3. Radiat. Phys. Chem. **242**, 113645 (2026)
21. C. Hao, L. Wang, F. Wen, J. Xiang, L. Li, W. Hu, Z. Liu, Layer structured bismuth selenides Bi_2Se_3 and Bi_3Se_4 for high energy and flexible all-solid-state micro-supercapacitors. Nanotechnology. **29**, 085401 (2018)
22. A. Moyseowicz, Scalable one-pot synthesis of bismuth sulfide nanorods as an electrode active material for energy storage applications. J. Solid State Electrochem. **23**, 1191–1199 (2019)
23. K. Namsheer, S. Thomas, A. Sharma, S.A. Thomas, K.A. Sree Raj, V. Kumar, A. Gagliardi, A. Aravind, C.S. Rout, Rational design of selenium inserted 1T/2H mixed-phase molybdenum disulfide for energy storage and pollutant degradation applications. Nanotechnology. **33**, 445703 (2022)
24. J. Lin, S. Lu, Y. Zhang, L. Zeng, Y. Zhang, H. Fan, Selenide-doped bismuth sulfides ($Bi_2S_{3-x}Se_x$) and their hierarchical heterostructure with ReS_2 for sodium/potassium-ion batteries. J. Colloid Interface Sci. **645**, 654–662 (2023)
25. H. Qin, Y. Lv, P. Li, M. Xiao, H. Song, Q. Zhang, J. Yang, Bismuth metal organic framework-derived Bi_2Se_3@C for high performance supercapacitors. New J. Chem. **45**, 21888–21895 (2021)
26. P. Simon, Y. Gogotsi, B. Dunn, Where do batteries end and supercapacitors begin? Science. **343**, 1210–1211 (2020)
27. V. Augustyn, P. Simon, B. Dunn, Pseudocapacitive oxide materials for high-rate electrochemical energy storage. Energy Environ. Sci. **13**, 1597–1614 (2020)
28. J.B. Goodenough, K.S. Park, The Li-ion rechargeable battery: A perspective. J. Am. Chem. Soc. **142**, 19113–19129 (2020)
29. X. Wang, L. Lu, Y. Li, J. Sun, T. Zhai, Flexible energy-storage devices: Design consideration and recent progress. Adv. Mater. **33**, 2002395 (2021)
30. E.S. Bidhan Pandit, H. Goda, Mahmoud, Abu, Elella et al., Aafaq ur Rehman, One-pot hydrothermal preparation of hierarchical manganese oxide nanorods for high-performance symmetric supercapacitors, Journal of Energy Chemistry. 65 (2022) 116–126
31. A.P. Khedulkar, B. Pandit, W.-J. Yu, Ruey-an Doong, Urchin-like Ni-Co hydroxide@tamarind seed biochar for high performance supercapacitor. J. Energy Storage. **84**, 110639 (2024)
32. S. Emad, Goda, Aafaq ur Rehman, Bidhan Pandit, Ahmed Al-Shahat Eissa,Sang Eun Hong, Kuk Ro Yoon, Al-doped Co_9S_8 encapsulated by nitrogen-doped graphene for solid-state asymmetric supercapacitors. Chem. Eng. J. **428**, 132470 (2022)
33. S. Chen, L. Shen, P.A. van Aken, X. Maier, Y. Yu, Advanced nanostructured materials for high-performance supercapacitors. Chem. Eng. J. **420**, 127660 (2021)
34. X. Zhang, Y. Liu, H. Wang, J. Chen, Surface-controlled pseudocapacitive charge storage in chalcogenide-based electrode materials for high-rate energy storage. J. Alloys Compd. **965**, 183093 (2025)
35. K. Pranav, Z.A. Katkar, S.-W. Sheikh, Lee, Fabrication of 3D hierarchically porous Cu-Cr phosphate@MWCNTs nanocomposites for hybrid solid-state energy storage. J. Alloys Compd. **1039**, 183093 (2025)
36. P.K. Katkar, S.-H. Chun, S.-W. Lee, Rational design and electrochemical characterization of a 3D cobalt phosphate/MXene/vertical graphene nanohills (VGNHs) heterostructure for supercapacitor applications. J. Alloys Compd. **1050**, 185907 (2026)
37. B.R. Bidhan Pandit, Sankapal, Cerium Selenide Nanopebble/Multiwalled Carbon Nanotube Composite Electrodes for Solid-State Symmetric Supercapacitors, ACS Appl. Nano Mater. **5**, 3007–3017 (2022)
38. M. Hamdan, T.M. Danamah, V.V. Al-Hejri, T.A.J. Jadhav, S.F. Siddiqui, S. Shaikh, Abu ul Hassan, R.S. Rana, Mane, Chemical synthesis of Bi_2O_3 and its ionic conversion to Bi_2S_3, Bi_2Se_3, and $Bi_2S_{3x}Se_{3(x-1)}$ nanostructures as high-performance electrochemical supercapacitors. J. Power Sources. **652**, 237301 (2025)
39. B. KaniAmuthan, R. Ponnusamy, A. Karuppannan, U. Jethawa, R. Venkatesan et al., Scalable synthesis of Bi_2S_3/Se fused nanoplatelets with promising super-capacitive performance. J. Power Sources. **650**, 237490 (2025)
40. L. Jin Liu, J. Ren, H. Luo, Li, Composites of Bi_2Se_3 nanoparticles and $FeSe_2$ nanoparticles for supercapacitor anode materials. Mater. Res. Bull. **174**, 112738 (2024)
41. Q.-X. Ma, M.-Z. Chen, K. Wang, T. Song, Q. Wang, H.-L. Zhang, Scalable fabrication of two-dimensional Bi_2Se_3 for high-performance supercapacitors. Mater. Res. Bull. **175**, 112753 (2024)

42. Kalyan Ghosh, Superior supercapacitor performance of Bi_2S_3 nanorod/reduced graphene oxide composites. Dalton Trans. **49**, 16993–17004 (2020)
43. H. Qin, Y. Lv, P. Li, M. Xiao, H. Song, Q. Zhang, J. Yang, Bismuth metal organic framework-derived Bi_2Se_3@C for high performance supercapacitors. New. J. Chem. **45**, 21888–21895 (2021)
44. R. Jyoti, J. Sharma, Deepeka, S. Singh, S. Singhal, Rana, Interfacial engineering of biomass-supported Bi_2S_3 and Ce-doped Co_3O_4 electrodes for high-rate asymmetric energy storage devices. Surf. Interfaces. **87**, 108992 (2026)
45. Q.-X. Ma, M.-Z. Chen, K. Wang, T. Song, Q. Wang, H.-L. Zhang, Scalable fabrication of two-dimensional Bi_2Se_3 for high-performance supercapacitors. Mater. Res. Bull. **175**, 112753 (2024)
46. S.A. Ahmad, M. Arif, I. Hussain, Y. Liu, W. Zhang, T. Zhu, Integrating ZnS microspheres with Bi_2Se_3 sponge ball structures to realize high energy density with good stability for supercapacitors. APL Mater. **13**, 051107 (2025)
47. K. Pranav, Z.A. Katkar, V.D. Sheikh, Chavan, Sang-Wha Lee, In-situ growth of 3D amorphous Ni-Co-Mn phosphate on 2D Ti_3C_2Tx nanocomposite for commercial-level hybrid energy storage application. J. Mater. Sci. Technol. **206**, 282–296 (2025)
48. G. Kuladip, S.S. Belekar, S.B. Patil, S.S. Bhosale, G.D. Kumbhar, Jadhav, Amorphous, binder-free cobalt manganese phosphate cathodes prepared by SILAR method for asymmetric supercapacitors: Harnessing cationic synergy. Synth. Met. **311**, 117800 (2025)
49. K. Pranav, M.B. Katkar, -W. Naikwade, Lee, A synergistic electrochemical properties of 3D marigold-like Fe-Cu-Ag phosphate/MWCNTs nanocomposite towards hybrid solid-state supercapatteries. J. Alloys Compd. **1038**, 182815 (2025)

Publisher's note Springer Nature remains neutral with regard to jurisdictional claims in published maps and institutional affiliations.

Springer Nature or its licensor (e.g. a society or other partner) holds exclusive rights to this article under a publishing agreement with the author(s) or other rightsholder(s); author self-archiving of the accepted manuscript version of this article is solely governed by the terms of such publishing agreement and applicable law.